



# Investigation of structural, morphological and magnetic study of Ni–Cu-substituted $\text{Li}_{0.5}\text{Fe}_{2.5}\text{O}_4$ ferrites

D. Parajuli<sup>1,2</sup> · N. Murali<sup>3,4</sup> · Vemuri Raghavendra<sup>5</sup> · B. Suryanarayana<sup>6</sup> · Khalid Mujasam Batoo<sup>7</sup> · K. Samatha<sup>8</sup>

Received: 7 January 2023 / Accepted: 24 May 2023 / Published online: 22 June 2023  
© The Author(s), under exclusive licence to Springer-Verlag GmbH, DE part of Springer Nature 2023

## Abstract

The  $\text{Li}_{0.5-x}\text{Ni}_x\text{Cu}_x\text{Fe}_{2.5-x}\text{O}_4$  for  $x = 0.00, 0.05, 0.10, 0.15, 0.20,$  and  $0.25$  were synthesized through the ceramic process following double sintering. Their structural, morphological, compositional, functional, and magnetic properties were analyzed with the help of X-ray diffraction (XRD), Scanning Electron Microscopy (SEM), Energy Dispersive X-ray Spectroscopy (EDS), Fourier Transform Infrared Spectroscopy (FTIR), and Vibrating Sample Magnetometer (VSM). The XRD patterns confirmed the single-phase spinel cubic structure. Lattice parameters increase from  $8.3558 \text{ \AA}$  to  $8.3615 \text{ \AA}$ . The increase in lattice parameter suggests the occupancy of Cu ions in the tetrahedral site, which can also be seen from the FTIR spectrum between  $390$  and  $580 \text{ cm}^{-1}$ . The SEM images show the grain size in the  $2.28$  to  $3.75 \text{ \mu m}$ , whereas the porosity ranges between  $4.4\%$  and  $9.7\%$ . A squareness ratio ranges between  $0.18$  and  $0.24$ ; the specific magnetization is between  $26$  and  $42 \text{ emu/g}$ . The coercivity is observed to range between  $138 \text{ Oe}$  and  $145.75 \text{ Oe}$ . The attached EDS spectra show the composition of the samples that agree well with their stoichiometry. The VSM study shows the occupancy of copper on both A- and B-sites as observed by cation distribution. Low electric and magnetic loss, low ac conductivity, and temperature-independent electric and magnetic properties are the fundamental properties of microwave devices that were obtained for the considered composition. Therefore, the substitution gives rise to the ferrite, which is appropriate for microwave devices.

**Keywords** Lithium ferrite · Scanning electron microscopy (SEM) · Cation distribution · Vibrating sample magnetometer (VSM) · Microwave materials

✉ N. Murali  
muraliphda@gmail.com

<sup>1</sup> Research Center for Applied Science and Technology, Tribhuvan University, Kathmandu, Nepal

<sup>2</sup> Department of Physics, Tri-Chandra Multiple Campus, Kathmandu, Nepal

<sup>3</sup> Department of Engineering Physics, AUCE (A), Andhra University, Visakhapatnam, India

<sup>4</sup> Faculty of Allied Health Sciences, Chettinad Hospital Research Institute, Chettinad Academy of Research and Education, Kelambakkam, Tamil Nadu 603103, India

<sup>5</sup> Department of Physics, Sri Venkateswara College, Benito Juarez Marg, Dhaulikaun, New Delhi 110021, India

<sup>6</sup> Department of Basic Science and Humanities, Raghu Engineering College (A), Dakamarri, Bheemunipatnam Mandal, Visakhapatnam, Andhra Pradesh, India

<sup>7</sup> College of Science, King Saud University, P.O. Box-2455, Riyadh 11451, Saudi Arabia

<sup>8</sup> Department of Physics, College of Science and Technology, Andhra University, Visakhapatnam, India

## 1 Introduction

However, expensive, yttrium iron garnets (YIG), low Curie temperature, lower magnetic saturation, etc., are the microwave materials used in memory cores, circulars, isolators, gyrators, phase shifters, etc. Hexagonal ferrites have promising properties, such as dielectric, magnetic and superconducting, making them suitable for practical uses [1–6]. Lithium ferrites and their derivatives are becoming alternative materials due to their higher frequency performance with low losses [7–10]. Highly resistive materials with low dielectric losses and appropriate saturation magnetization are preferable for microwave devices [9]. Lithium ferrites are also studied for their application in energy storage applications [11–13]. They are chemically and thermally stable, with low losses in magnetism and eddy current [14]. There is still a need for such cheap and quality microwave materials to work efficiently at high frequencies. The ions' nature and cations distribution in the two interstitial sites plays an essential role in the device's performance. Ferrites have

higher magnetic saturation of around 3550 Gauss and Curie temperature of around 640 °C.

Some efforts were made with the substitution ions with two, three, and four oxidation states [15, 16]. Since lithium ferrite is a spinel ferrite and these materials are observed to be promising materials for several practical applications [17–19]. Different substitutions (Ti, Zn, Cd, etc.) have been observed in the lithium ferrites to modify the properties of lithium ferrites. Since a couple of years ago, we have been conducting several experimental works on other ferrite materials Ni–Zn ferrites [20–25] and Co–Cu ferrites [26, 27]. We have doped Ni in Co–Cu and found the material compatible with the spin transistor [27]. However, the efficiency of microwave devices from such works was not significant. Continuing that work, we are working further on those microwave materials.

Aravind et al. reported the lithium nickel ferrite nanoparticles by the low-temperature citrate gel auto-combustion method. They noted the decrease in saturation magnetization from 56 emu/g to 28 emu/g with increased Ni<sup>2+</sup> ions concentration [28]. Similarly, Venketochalapathy et al. synthesized Ni and Al-doped lithium ferrite nanoparticles and observed that saturation magnetization decreased from 48.3 emu/g to 46.2 emu/g. A noticeable change is also observed in the coercivity of the prepared sample [29]. Thus, Nickel, a ferrimagnetic metal, can be magnetized easily, even at room temperature and can act as a suitable dopant to improve the magnetic properties. In addition, Cu<sup>2+</sup> ions are paramagnetic, and their doping can favour the appearance of a superparamagnetic ground state at room temperature. The Cu<sup>2+</sup> (d9) ion in the 3d transition metal group is well-known for its metallic and paramagnetic behaviour. Thus, the presence of Cu<sup>2+</sup> ions in the octahedral environment of spinel ferrites minimises the system's overall energy [30, 31]. Ramesh et al. 2019 investigated the cation distribution of these ferrites [32].

The above discussion shows that lithium ferrite has exceptional properties, and Nickel and Copper can readily improve spinel ferrite's magnetic and structural properties. Thus, observing the effect of Ni and Cu doping on lithium ferrite becomes an interesting topic. In this work, we have studied the structural, morphological, compositional, functional, and magnetic properties of nickel- and copper-substituted lithium ferrite using XRD, SEM–EDS, FTIR, and VSM to improve their electromagnetic properties.

## 2 Materials and methods

The Li<sub>0.5-x</sub>Ni<sub>x</sub>Cu<sub>x</sub>Fe<sub>2.5-x</sub>O<sub>4</sub> for  $x = 0.00, 0.05, 0.10, 0.15, 0.20$  and  $0.25$  were synthesized through the ceramic process followed by double sintering. For that, Li<sub>2</sub>(CO)<sub>3</sub>, CuO, and Fe<sub>2</sub>O<sub>3</sub> were used as precursors with an analytical grade of the highest purity (> 99%). Precursors were

mixed with methanol in a mortar pestle. Obtained powders were calcinated at 750 °C for 6 h and then cooled naturally. The resultant powders were mixed with 5% PVA as a binder to form the pellets of cylindrical and toroidal shape with the help of a hydraulic press of 5 tons. The pellets were sintered at 1000 °C for 8 h. The powder was used for structural analysis through XRD incorporated with Cu–K $\alpha$  radiation, SEM–EDS, FTIR, and the pellets were used for the magnetic properties analysis through VSM.

## 3 Results and discussion

### 3.1 X-ray diffraction studies

The X-ray diffraction pattern of Li<sub>0.5-x</sub>Ni<sub>x</sub>Cu<sub>x</sub>Fe<sub>2.5-x</sub>O<sub>4</sub> for  $x = 0.00, 0.05, 0.10, 0.15, 0.20$  and  $0.25$  are shown in Fig. 1. For the concentration  $x = 0.00$ , it is simply Fe<sub>2</sub>O<sub>3</sub> (Hematite with antiferromagnetic nature) having some additional peaks (210), (211), (310), (321), and (421) along with (220), (311), (400), (422), (511), and (440). As the concentration increases, the phase changes slightly, disappearing the additional peaks seen at  $x = 0.00$ , which finally disappeared for concentration  $x = 0.20$ . The initial phase with space group P4<sub>1</sub>32 is changed into the Fd<sub>3</sub>m. These are the essential characteristics of lithium ferrites.

Substituting Li and Fe with Ni and Cu makes the hematite a cubic spinel. However, some initial peaks (210), (310), etc.) in the patterns show that the spinel still has an additional secondary hematite phase.

a) Observed lattice parameter

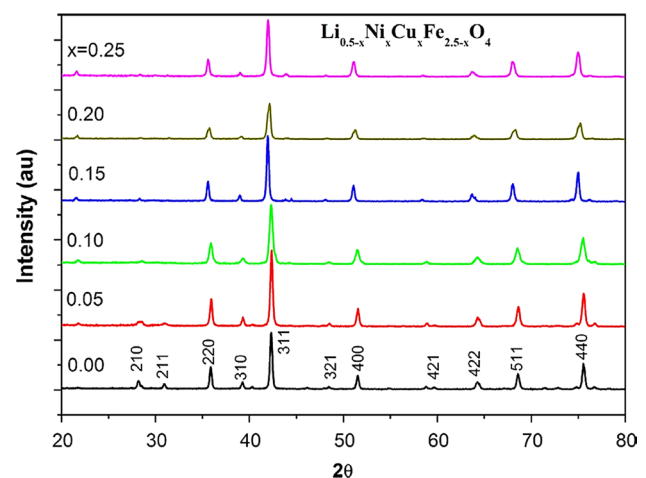


Fig. 1 XRD of Ni–Cu-substituted lithium ferrites

The Nelson–Riley error function was plotted against the lattice parameter to get a minimum error with the help of prominent peaks (220), (311), (400), (422), (511), and (440) of the samples [33]. The rising straight lines were obtained, which can be extrapolated to get the observed value showing the increasing lattice parameter (up to  $x = 0.10$ ) with concentration. The increase in the lattice parameter is due to the larger ionic radii of the substituted elements ( $\text{Ni}^{2+} - 0.069 \text{ nm}$  and  $\text{Cu}^{2+} - 0.073 \text{ nm}$ ) than that of the host elements ( $\text{Li}^+ - 0.073 \text{ nm}$  and  $\text{Fe}^{3+} - 0.0645 \text{ nm}$ ). The observed and calculated values are plotted in the graph, as shown in Fig. 2. The larger ion gives rise to the lattice strain and changes its elastic property, thereby changing the interplanar spacing and the diffraction peak shifting towards the lower angle side [34, 35]. The symmetry of the lattice is preserved as indicated by the uniform increase in lattice parameter and hence the volume of the unit cell to accommodate the larger ion [36] as is reported in the previous literature [37].

### b) Theoretical lattice parameter

The difference between the theoretical and observed lattice parameters is mainly due to the cation distribution [12], as cations have different sizes for site occupancy. e. g.,  $\text{Cu}^{2+}$  ions have a tetrahedral radius of  $0.57 \text{ \AA}$  and an octahedral radius of  $0.73 \text{ \AA}$  due to their fourfold and sixfold coordination, respectively. Therefore, careful assignment of the cations in the respective site is necessary to have the exact reason and value of the lattice parameter. The assignment of the cations on the site is listed in Table 1. The value of the lattice constant is determined theoretically by [38]

**Table 1** Cation distribution of LNC series (proposed)

$x$	A site	B site
0.00	Fe	$\text{Li}_{0.5}\text{Fe}_{1.50}$
0.05	Fe	$\text{Li}_{0.45}\text{Ni}_{0.05}\text{Cu}_{0.05}\text{Fe}_{1.45}$
0.10	Fe	$\text{Li}_{0.40}\text{Ni}_{0.10}\text{Cu}_{0.10}\text{Fe}_{1.40}$
0.15	$\text{Fe}_{0.97}\text{Cu}_{0.03}$	$\text{Li}_{0.35}\text{Ni}_{0.15}\text{Cu}_{0.12}\text{Fe}_{1.38}$
0.20	$\text{Fe}_{0.94}\text{Cu}_{0.06}$	$\text{Li}_{0.30}\text{Ni}_{0.20}\text{Cu}_{0.20}\text{Fe}_{1.36}$
0.25	$\text{Fe}_{0.90}\text{Cu}_{0.10}$	$\text{Li}_{0.25}\text{Ni}_{0.25}\text{Cu}_{0.15}\text{Fe}_{1.35}$

$$a_{th} = \frac{8}{3\sqrt{3}}(r_A + R_o) + (r_B + R_o)$$

Here,  $r_A$ ,  $r_B$ , and  $R_o$  are the mean radii of the A site, B site, and oxygen ion. The  $r_A$  and  $r_B$  of the LNC series can be calculated using the following expressions [38].

$$r_A = (y)r_{\text{ACu}2+} + (1 - y)r_{\text{AFe}3+}$$

$$r_B = \frac{1}{2}(0.5 - x)r_{\text{BLi}+} + (xr)r_{\text{BNi}2+} + (x - y)r_{\text{BCu}2+} + \frac{1}{2}(1.5 - x + y)r_{\text{BFe}3+}$$

Both (A and B site) ionic radii of  $\text{Li}^+$ ,  $\text{Ni}^{2+}$ ,  $\text{Cu}^{2+}$ , and  $\text{Fe}^{3+}$  are taken from Shannon 1970 [34]. Table 2 gives a comparison between the calculated and experimental lattice constant values. The same has been shown as a graph for easily depicting the trends in Fig. 2.

Figure 3 shows the Williamson–Hall plot for all the prepared samples. All the samples show anisotropic behaviour. The lattice strain and crystallite size are estimated from the Williamson–Hall plots and presented in Table 3. The lattice strain increased till  $x = 0.10$  and further decreased. For  $x = 0.25$ , the strain is compressive. The highest strain is observed for  $x = 0.10$ , which is due to the large number of Cu ions at the B-site and afterwards, the Cu ions start distributing over both the A-site and B-site. The crystallite size increases with the concentration of dopants till  $x = 0.1$ , after which it decreases.

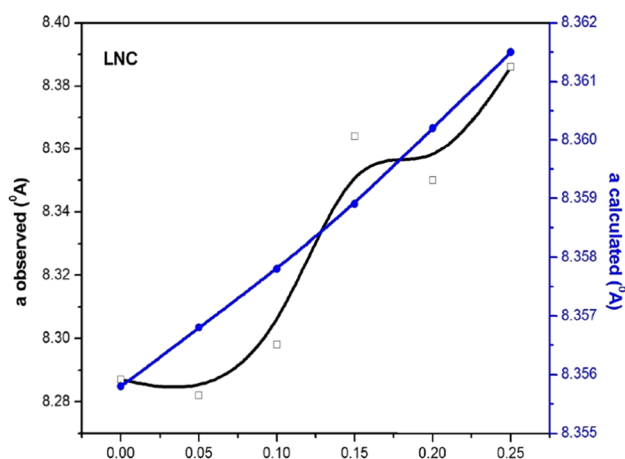


**Fig. 2** Comparison of variations of observed and calculated LNC lattice constants with concentration ( $x$ )

**Table 2** Experimental and calculated lattice constants of  $\text{Li}_{0.5-x}\text{Ni}_x\text{Cu}_x\text{Fe}_{2.5-x}\text{O}_4$  (LNC series)

$x$	$a_{\text{obs}}$ (Å)	$a_{\text{cal}}$ (Å)
0.00	8.287	8.3558
0.05	8.282	8.3568
0.10	8.298	8.3578
0.15	8.364	8.3589
0.20	8.350	8.3602
0.25	8.386	8.3615

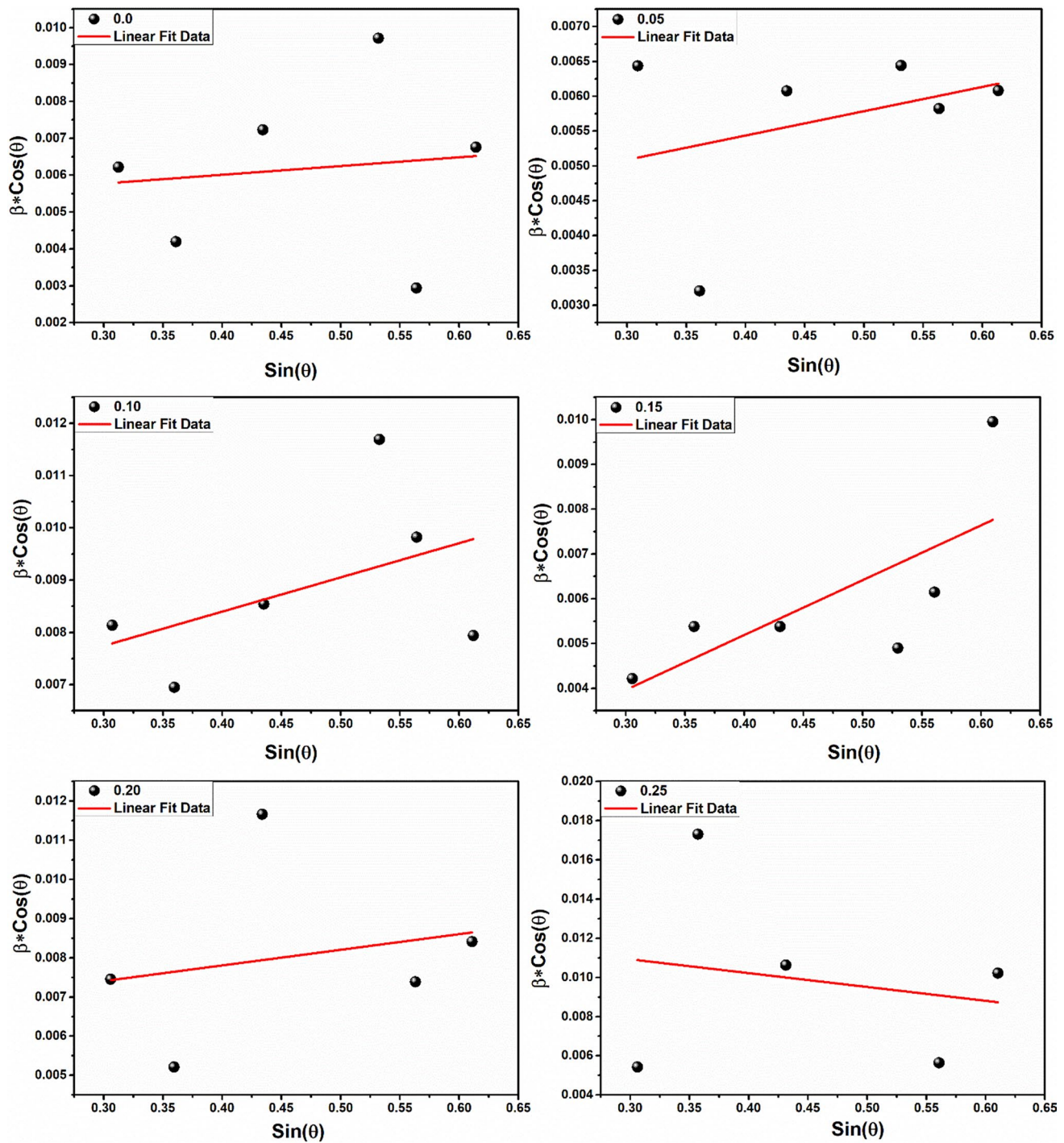


Fig. 3 Williamson–Hall plot for  $\text{Li}_{0.5-x}\text{Ni}_x\text{Cu}_x\text{Fe}_{2.5-x}\text{O}_4$  (LNC series)

### 3.2 Microstructural studies by SEM

The SEM micrographs of  $\text{Li}_{0.5-x}\text{Ni}_x\text{Cu}_x\text{Fe}_{2.5-x}\text{O}_4$  for

$x = 0.00, 0.05, 0.10, 0.15, 0.20,$  and  $0.25$  are shown in Fig. 4. The grain distribution seems to be distributed homogeneously and almost without agglomeration. The size of the grains increases with concentration showing its possible effect on the properties, viz., electrical and



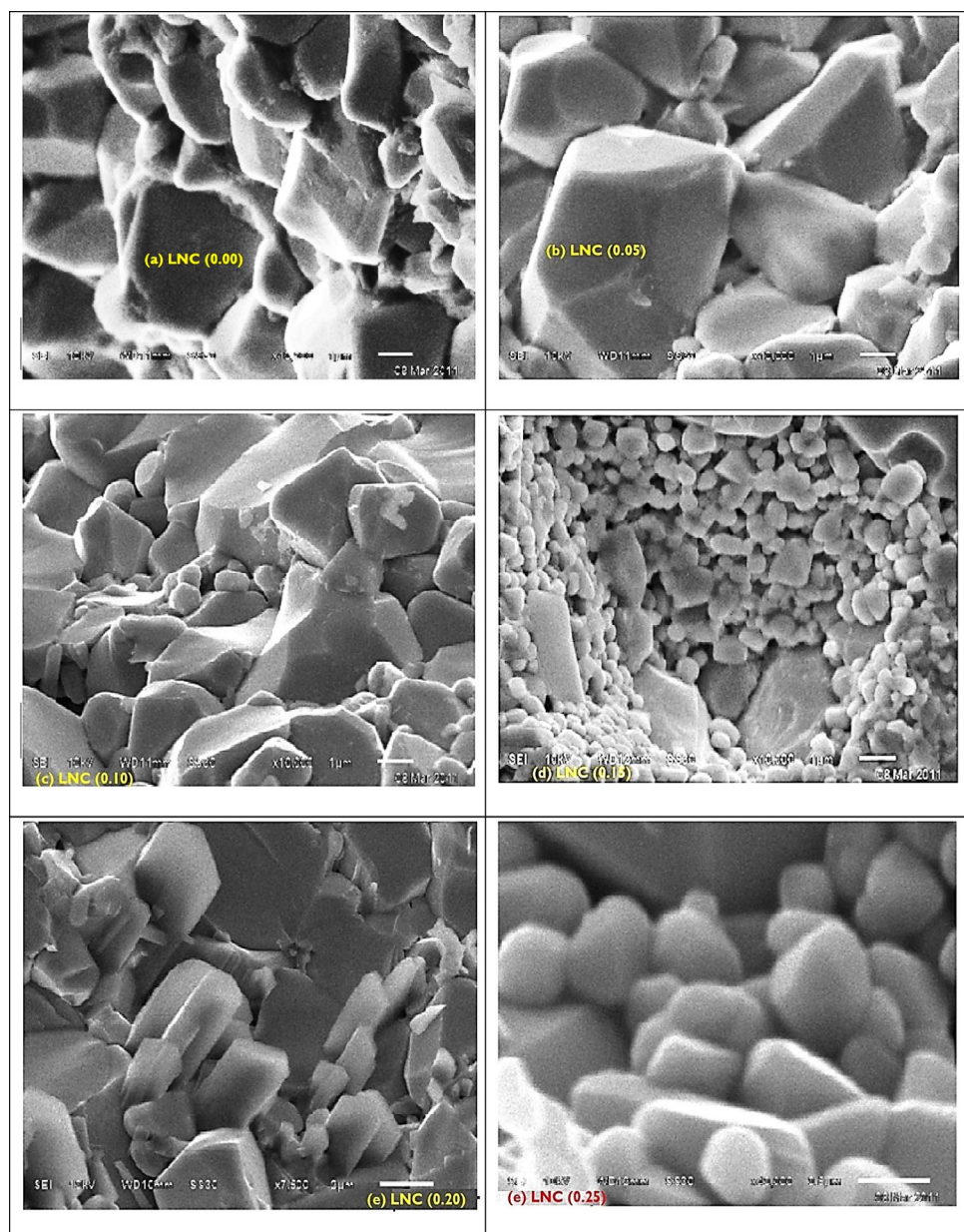
**Table 3** Crystallite size and lattice strain values estimated from Williamson–Hall plot for all the sample

$x$	Crystallite size ' $d$ ' (nm)	Lattice strain ( $\epsilon$ )
0.0	27.39	0.00396
0.05	29.31	0.00316
0.10	33.91	0.00493
0.15	27.56	0.00324
0.20	22.31	0.00263
0.25	11.63	-0.00706

magnetic of the sample. These grain size variations are used to determine the magnetic and resistive properties.

### 3.3 EDS study

The allocation of the two absorption studied with the help of energy-dispersive spectroscopy (Phillips XL30 ESEM), and the spectra obtained are shown in Fig. 5. The figure shows that the sample contains Ni, Cu, Fe, and O elements in their stoichiometry ratio (the Ni and Cu are not present for  $x = 0.00$ ). The atomic and weight percentage is also presented in Table 4, which shows the presence of all the elements, and their weight percentage signifies the chemical purity of all the samples.

**Fig. 4** SEM images of the LNC series

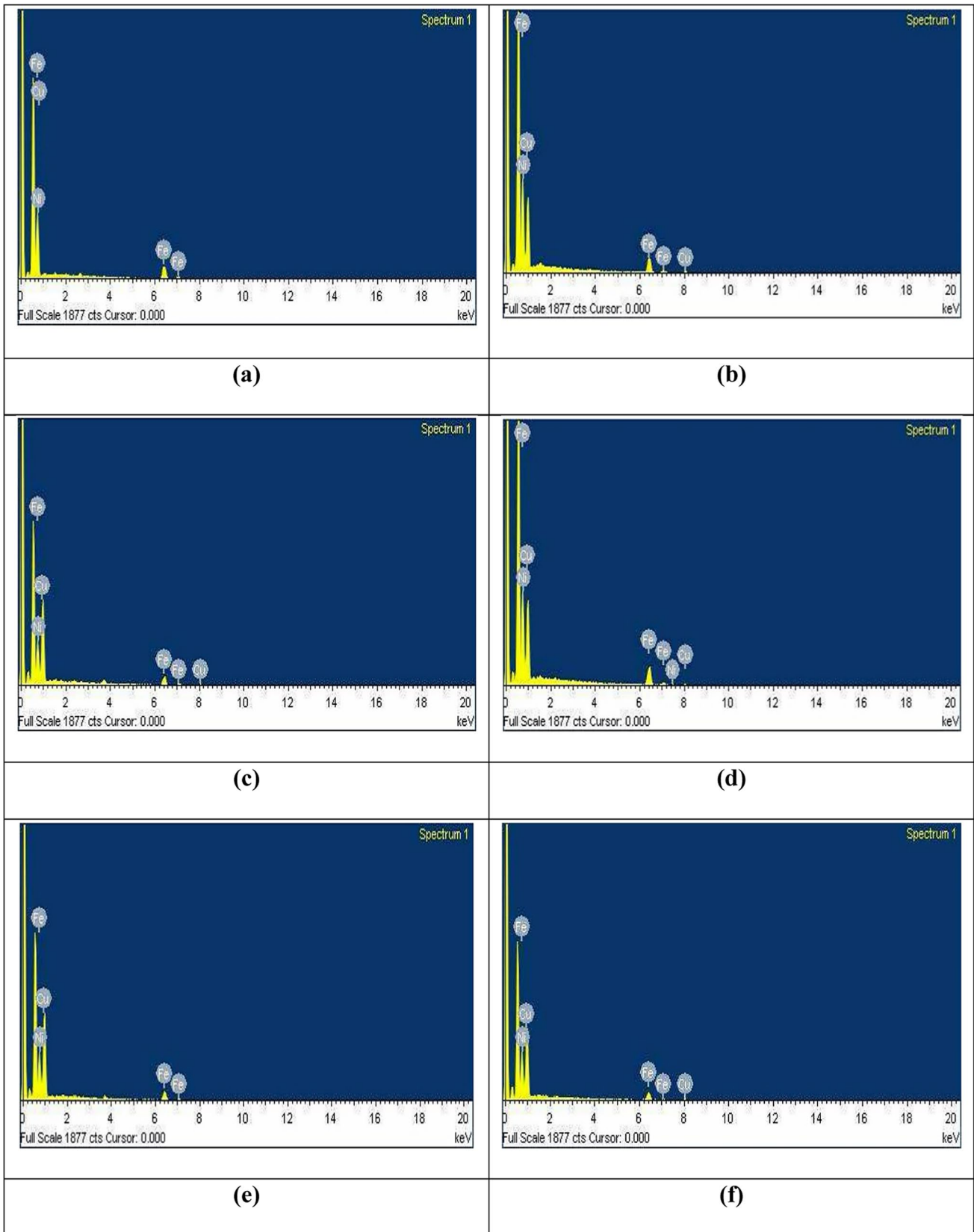


Fig. 5 EDS spectra of LNC series of samples

**Table 4** Atomic percentage and weight percentage of elements in  $\text{Li}_{0.5-x}\text{Ni}_x\text{Cu}_x\text{Fe}_{2.5-x}\text{O}_4$ 

$x$	0.00 (%)	0.05 (%)	0.10 (%)	0.15 (%)	0.20 (%)	0.25 (%)
Wt% of Li	1.62	1.49	1.36	1.23	1.10	0.97
Wt% of Ni	0.00	0.63	1.26	1.88	2.51	3.14
Wt% of Cu	0.00	0.63	1.26	1.88	2.51	3.14
Wt% of Fe	67.48	65.14	62.80	60.46	58.12	55.78
Wt% of O	30.80	30.47	30.14	29.81	29.48	29.15
Atomic % of Li	7.14	6.47	5.81	5.14	4.48	3.81
Atomic % of Ni	0	0.72	1.45	2.17	2.89	3.62
Atomic % of Cu	0	0.72	1.45	2.17	2.89	3.62
Atomic % of Fe	35.71	35.25	34.79	34.33	33.87	33.41
Atomic % of O	57.14	57.84	58.50	59.16	59.81	60.47

### 3.4 FTIR characterization

The FTIR spectra of the LNC sample taken at room temperature in the range of  $300\text{--}750\text{ cm}^{-1}$  are shown in Fig. 6. The allocation of the two absorption peaks around  $580\text{ cm}^{-1}$  ( $\nu_1$ ) and another around  $390\text{ cm}^{-1}$  ( $\nu_2$ ) shows their spinel structure.

The octahedral band is central and is shifted towards the higher frequency side between  $x = 0.10$  to  $0.20$  with the increase in concentration. The shoulder peaks  $\nu_{2s_1}$  and  $\nu_{2s_2}$  arise due to its (B site) divalent metal ion–oxygen system [39], and  $\nu_{1s_1}$  and  $\nu_{1s_2}$  arise due to divalent metal ion–oxygen complexes in the A-site. The values of  $\nu_1$ ,  $\nu_2$ ,  $\nu_{1s_1}$ ,  $\nu_{1s_2}$ ,  $\nu_{2s_1}$ , and  $\nu_{2s_2}$  are listed in Table 5.

Waldron et al. showed that the vibration of cubic spinel unit cells could be generated in the two sites that cause the stretching of the metal–oxygen bonds of the respective sites [40]. The bond length in the two sites ( $\text{Fe}^{3+}\text{--O}^{2-}$  in the A site is  $1.89\text{ \AA}$  and  $\text{Fe}\text{--O}$  in the B site) is different, so the vibration frequency is also different [41]. The smaller length gives rise to a more significant frequency making the central band move towards the larger frequency. This takes place in the concentration between  $0.10$  and  $0.20$ . Therefore, an increase in frequency indicates a decrease in bond length which further indicate the occupancy of Copper ion in the respective site [42].

In addition, the bands are wider on the substitution of Ni–Cu elements. The variation of wave number and ionic radii with concentration for tetrahedral and octahedral sites are shown in Figs. 7 and 8, respectively. The widening of the bands was due to the distribution of  $\text{Fe}^{3+}$  ions in both sites [38]. Furthermore, the intensity of the sample depends almost on cation distribution. Pure lithium and iron are found in a 1:3 ratio in the B site. The replacement of  $\text{Ni}^{2+}$  and  $\text{Cu}^{2+}$  ions by  $\text{Li}^{2+}$  and  $\text{Fe}^{3+}$  ions in both sites for concentrations beyond  $0.15$  and that from the B site creates disorders in the system which is indicated by the widening of the IF bands [43, 44]. The study shows the

necessity of the Ni and Cu substitution for their application in microwave devices.

### 3.5 Magnetic properties

#### a) Saturation magnetization

Figure 9 shows the room temperature hysteresis loops of the  $\text{Li}_{0.5-x}\text{Ni}_x\text{Cu}_x\text{Fe}_{2.5-x}\text{O}_4$  for  $x = 0.00$  to  $0.25$  in steps of  $0.05$ . The saturation magnetization decreased with concentration up to  $x = 0.01$  and then increased beyond. Furthermore, the lower coercivity indicates the nature of soft ferrite.

The change in the magnetic saturation with the substituent was due to the super-exchange interaction between the two interstitial sites, A and B [45, 46]. There are mainly three types of such interactions; AA, AB, and BA, among which AB interaction is most prominent. This gives rise to the alignment of magnetic spin in A and B in two opposite directions. As a result, the total magnetic moment is given by  $M = |M_B - M_A|$ . The ionic nature and valence state greatly affect the intensity of the exchange interactions [47, 48]. Junaid et al. observed that with the increase in Zr and Ni dopant concentration on lithium ferrite, saturation magnetization increased from  $9.52$  to  $19.31\text{ emu/g}$ , and coercivity decreased from  $2241.34$  to  $214.65\text{ Oe}$  and remnant magnetization increased from  $4.14$  to  $5.92\text{ emu/g}$  [49]. Mali et al. also observed the magnetic properties of Cr-doped lithium ferrite and observed that saturation magnetization decreased from  $71.1\text{ emu/g}$  to  $16.5\text{ emu/g}$  with increased chromium concentration [50]. Junaid et al. doped lithium ferrite with Indium and observed that saturation magnetization decreased from  $53.08$  to  $43.03\text{ emu/g}$ , coercivity increased from  $186.35$  to  $206.18\text{ Oe}$  and remnant magnetization decreased from  $12.52$  to  $8.78\text{ emu/g}$  [51].

However, in our samples, we observed a decrease in saturation magnetization at the first instance and then an increase in saturation magnetization with the increase in Nickel and copper.  $\text{Li}^+$  is a monovalent cation, and  $\text{Ni}^{2+}$  and  $\text{Cu}^{2+}$  ions

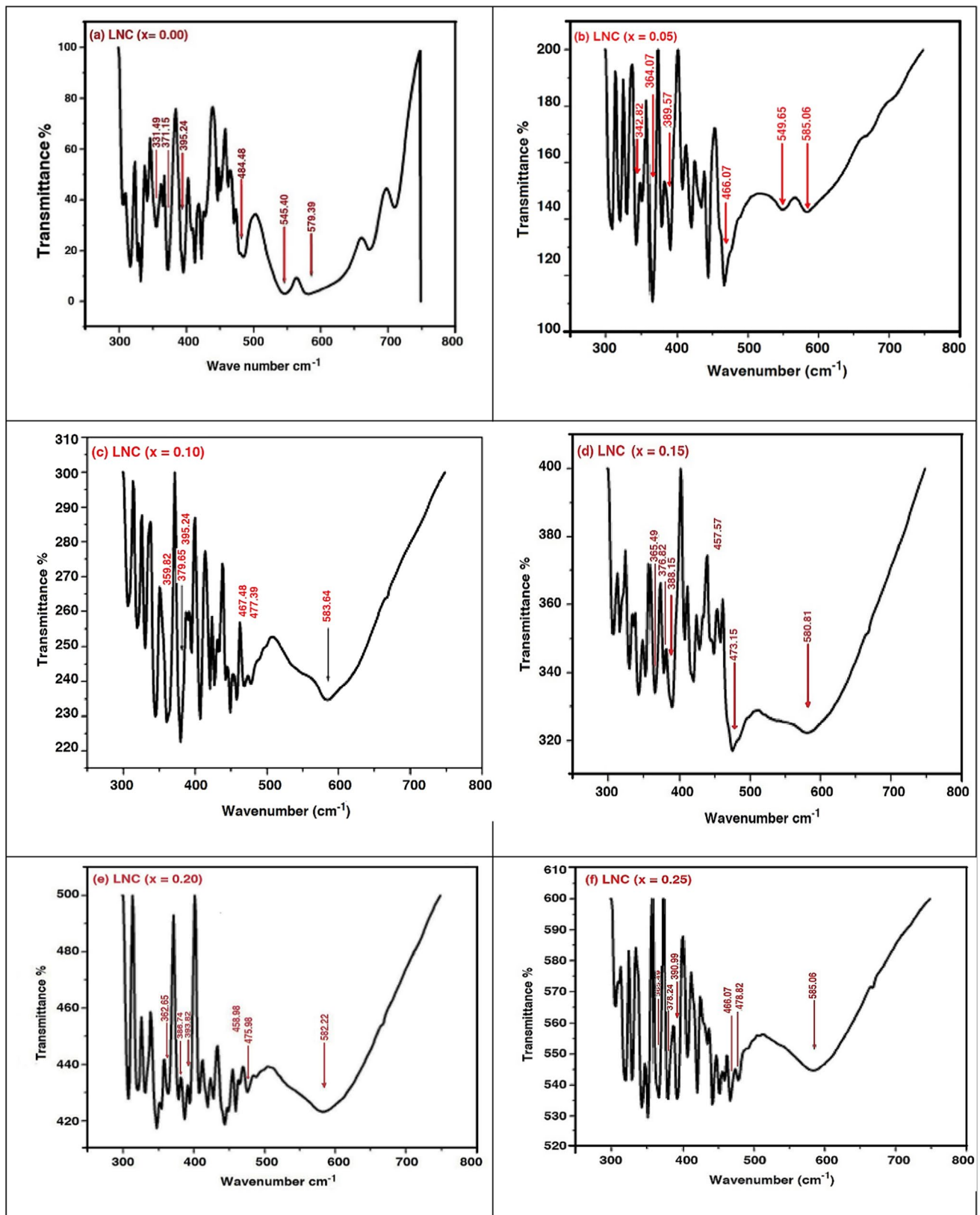
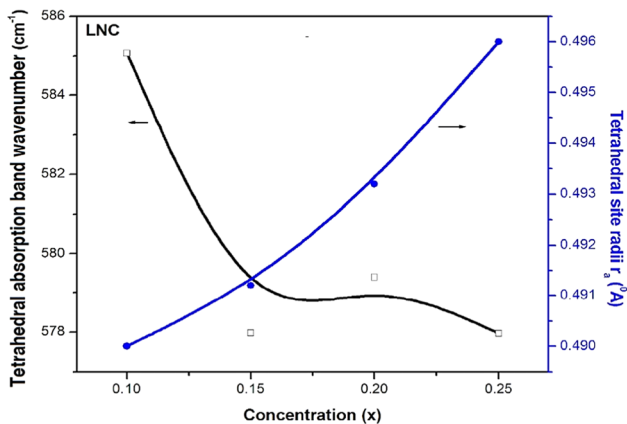
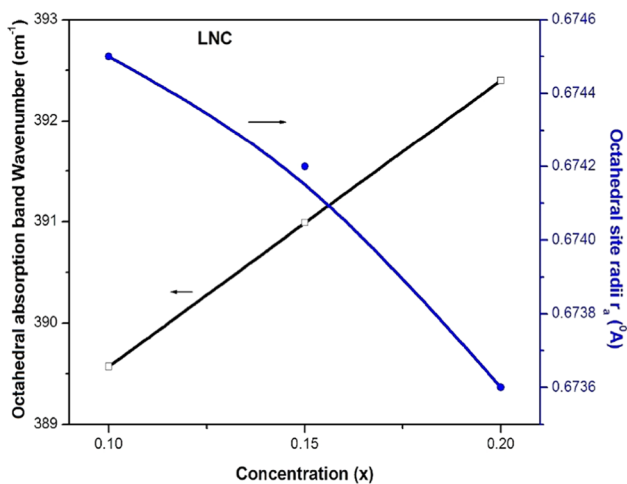


Fig. 6 FTIR spectrum of  $\text{Li}_{0.5-x}\text{Ni}_x\text{Cu}_x\text{Fe}_{2.5-x}\text{O}_4$ , where  $x = 0.00\text{--}0.25$

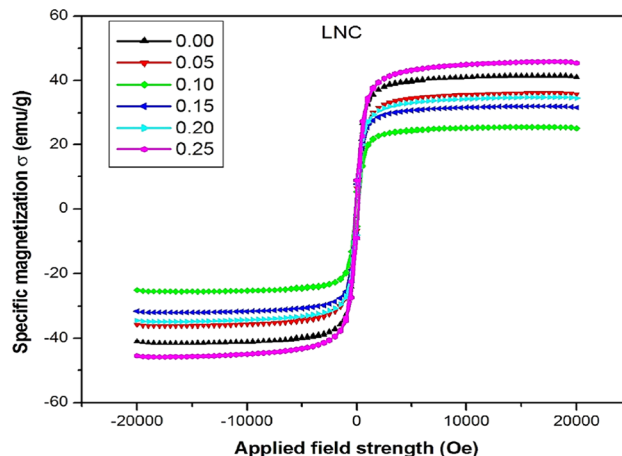


**Table 5** Vibrational frequencies variation with concentration ( $x$ ) in LNC series

$x$	$\nu_1$ (cm <sup>-1</sup> )	$\nu_{1s1}$ (cm <sup>-1</sup> )	$\nu_{1s2}$ (cm <sup>-1</sup> )	$\nu_2$ (cm <sup>-1</sup> )	$\nu_{2s1}$ (cm <sup>-1</sup> )	$\nu_{2s2}$ (cm <sup>-1</sup> )
0.00	579.39	545.40	484.48	395.24	371.15	331.49
0.05	585.06	549.65	466.07	389.57	364.07	342.82
0.10	583.64	477.39	467.48	395.24	379.65	359.82
0.15	580.81	473.15	457.57	388.15	376.82	365.49
0.20	582.22	475.98	458.98	393.82	386.74	362.65
0.25	585.06	478.82	466.07	390.99	378.24	365.49

**Fig. 7** Relation between absorption band wavenumber and site radius for tetrahedral sites in LNC series**Fig. 8** Plot of the octahedral band and radii against the concentration of dopants

are divalent. When divalent cations substitute monovalent cations, some higher spin Fe<sup>3+</sup> ions are transferred into lower spin Fe<sup>2+</sup> ions, decreasing saturation magnetization. However, with further doping  $x > 0.10$ , the Cu<sup>2+</sup> ions also started shifting to A-site, compensating for the formation of low-spin ions from high-spin ions and hence the saturation

**Fig. 9** Room temperature hysteresis loops of Li<sub>0.5-x</sub>Ni<sub>x</sub>Cu<sub>x</sub>Fe<sub>2.5-x</sub>O<sub>4</sub>

magnetization increases. Since, for the initial doping, Ni and Cu ions are present at B-site, and Fe<sup>2+</sup> ions are at A-site, affecting the magnetic behaviour of Fe<sup>3+</sup> ions. The Cu ions shift to A-site for higher concentrations, contributing to the A-B interaction. Table 6 shows the coercivity, grain size, porosity, saturation magnetization, remnant magnetization, and squareness ratio of the Ni–Cu lithium ferrite for different compositions ( $x$ ).

#### b) Effect of grain size on coercivity

The coercivity is decreased with an increase in grain size. This is due to the large number of domain walls in larger grain. The larger number of domain walls indicates their larger motion during magnetization or demagnetization, with a smaller field needed for rotation [52]. This means the coercivity is lower for larger grain sizes. The variation of coercivity and grain size with the concentration in the LNC series is shown in Fig. 10.

In the LNC series, one reason for the variation in the grain size and significant lowering of the coercivity was due to defects arising from maximum Cu ions substitution on the A site, and the other is due to the transfer of Fe ions to the B sites mainly for higher concentration.

#### iii) Effect of porosity on coercivity

**Table 6** Coercivity, grain size, porosity, saturation magnetization, remnant magnetization, and squareness ratio of the Ni–Cu lithium ferrite for different compositions (x)

x	Hc (Oe)	Grain size ( $\mu\text{m}$ )	Porosity (%)	Sat. Magn. (Ms) (emu/g)	Remnant Mag. (Mr) (emu/g)	Squareness ratio (Mr/Ms)
0.00	138.00	2.75	8.8	41.6	9.152	0.22
0.05	139.00	3.75	9.7	36.1	6.498	0.18
0.10	144.80	2.80	8.1	25.6	5.276	0.21
0.15	145.75	2.40	7.1	32.0	7.680	0.24
0.20	144.00	2.28	5.9	34.9	8.027	0.23
0.25	143.00	0.65	4.4	45.9	8.721	0.19

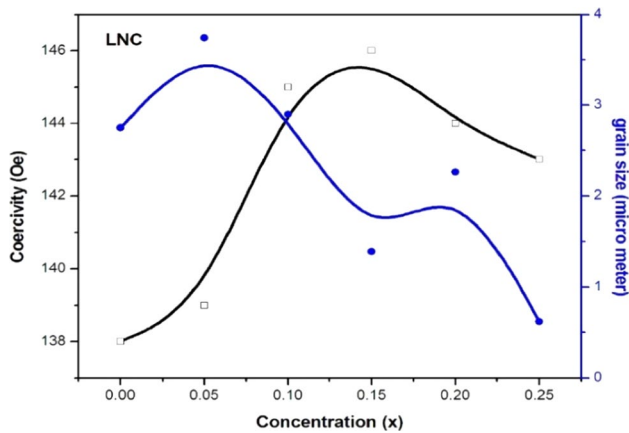


**Fig. 10** Variations of coercivity (Oe) and grain size ( $\mu\text{m}$ ) in LNC series

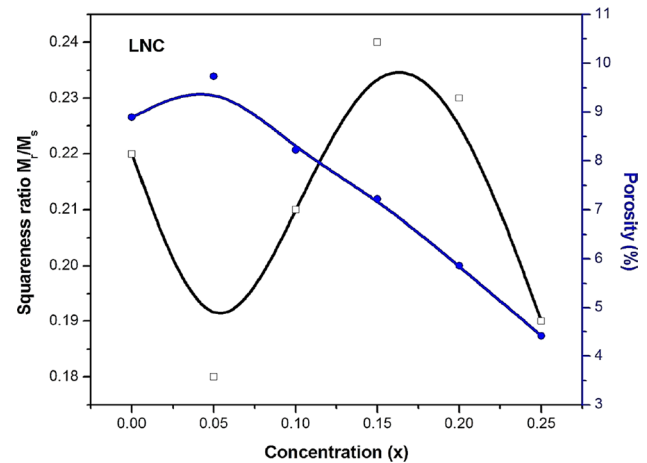


**Fig. 12** Variations of squareness ratio, coercivity, and porosity with concentration(x) in LNC series

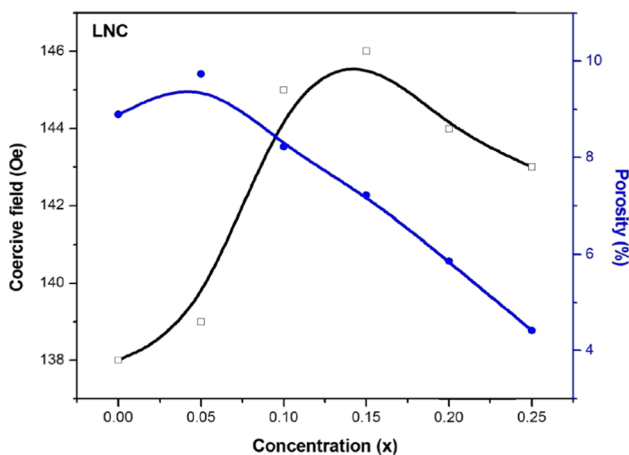


**Fig. 11** Coercive field and Porosity plot against concentration

The variations of the coercive field and the per cent porosity with concentration (x) in the LNC series are shown in Fig. 11. The change in the coercive field and porosity is in the same direction for higher and opposite direction for a lower concentration of Ni–Cu content as in the previous literature [53]. The different values for 0.25 are due to the structural defect arising from the

discontinuous growth of grains. The suitable intra-granular pores or phase plays an important role in increasing the grain sizes and hence the coercivity due to the solid magnetic isolation effect. It further indicates that a field required for rotating the domain wall is against the porosity amount [54].

#### iv) Effect of squareness ratio on porosity

The ratio of remnant magnetization (Mr) to the saturation magnetization (Ms) is the squareness ratio and is given by the Mr/Ms of the hysteresis loop. If the ratio value is around 0.5, the samples have a single magnetic domain system [53]. The present samples display squareness ratio values in the range of 0.18 to 0.26, typical of multidomain magnetic grains in the structure. This ratio is also directly proportional to the coercivity values and the per cent porosity data.

The variations in squareness ratio (Mr/Ms) and the porosity with concentration (x) for the LNC ferrite systems are shown in Fig. 12. This is attributed to the change in site preferences of Cu ions at higher concentrations, as discussed in the assigned cation distribution for this system.

## 4 Conclusions

In this report, we synthesized  $\text{Li}_{0.5-x}\text{Ni}_x\text{Cu}_x\text{Fe}_{2.5-x}\text{O}_4$  (where  $x = 0.00, 0.05, 0.10, 0.15, 0.20$  and  $0.25$ ) using a ceramic process followed by double sintering. XRD confirmed the formation of pure cubic spinel ferrite nanoparticles. Lattice parameters are observed to increase from 8.3558 Å to 8.3615 Å. The cation distribution and FTIR spectra suggested that Cu ions are distributed over A-site and B-site, whereas Ni ions are distributed over B-site. The SEM images showed the grain size within the 2.28 µm and 3.75 µm, whereas porosity was between 4.4% and 7.9%. The VSM analysis showed that saturation magnetization (Ms) ranges between 25.6 emu/g and 45.9 emu/g and coercivity in the 138 and 145.75 Oe ranges. The squareness ratio ranged between 0.18 and 0.24. The VSM analysis showed the occupancy of copper on both A and B sites. The substitution is observed to have a positive impact on lithium ferrite.

**Acknowledgements** The author, K M Batoo, would like to thank Researchers Supporting Project No. (RSP2023R148), King Saud University, Riyadh, Saudi Arabia, for financial support.

**Author contributions** All authors contributed to the study's conception and design. Material preparation, data collection and analysis were performed by DP, NM, VR, BS, KMB, KS. The first draft of the manuscript was written by NM, DP, and all authors commented on previous versions of the manuscript. All authors read and approved the final manuscript.

**Data availability** The corresponding authors' data supporting this study's findings are available upon reasonable request.

## Declarations

**Conflict of interest** The authors have no conflicts to disclose.

## References

1. Y. Slimani, B. Unal, M.A. Almessiere, E. Hannachi, G. Yasin, A. Baykal, I. Ercan, *J. Mater. Sci.* **31**, 7786–7797 (2020)
2. M.K.B. Salem, E. Hannachi, Y. Slimani, A. Hamrita, M. Zouaoui, L. Bessais, M.B. Salem, F.B. Azzouz, *Ceram. Int.* **40**, 4953–4962 (2014)
3. M.H.A. Mhareb, Y. Slimani, Y.S. Alajerami, M.I. Sayyed, E. Lacomme, M.A. Almessiere, *Ceram. Int.* **46**, 28877–28886 (2020)
4. A. Hamrita, Y. Slimani, M.K.B. Salem, E. Hannachi, L. Bessais, F.B. Azzouz, M.B. Salem, *Ceram. Int.* **40**, 1461–1470 (2014)
5. Y. Slimani, E. Hannachi, M.K.B. Salem, A. Hmarita, M.B. Salem, F.B. Azzouz, *J. Supercond. Nov. Magn.* **28**, 3001–3010 (2015)
6. M.A. Almessiere, Y. Slimani, H.S. El-Sayed, A. Baykal, *J. Rare Earth* **37**, 732–740 (2019)
7. P. Heide, *Microw. J.* **42**, 348 (1999)
8. J. S. Smit, H. P. J. Wijn, *Philips Tech. Libr.* (1961)\*\*\*
9. B. Lax, K.J. Button, *Microwave Ferrites And Ferrimagnetics* (McGraw-Hill, New York, 1962)
10. J. Nicolas, *Microwave Ferrites in Ferromagnetic Materials* (North-Holland, Amsterdam, 1980)
11. M. Ahmad, M. Shahid, Y.M. Alanazi, A.U. Rehman, M. Asif, C.W. Dunnill, *J. Mater. Res. Technol.* **18**, 3386 (2022)
12. D. Parajuli, N. Murali, K. Samatha, V. Veeraiah, *AIP Adv.* **12**, 085010 (2022)
13. D. Parajuli, P. Taddesse, N. Murali, V. Veeraiah, K. Samatha, *AIP Adv.* **12**, 125012 (2022)
14. W. Aulock, H. Von, A.S. Boxer, J.F. Ollom, R.F. Rauchmiller, *Handbook of Microwave Ferrite Materials* (Springer, Cham, 1965)
15. D.J. Craik (ed.), *Magnetic Oxides* (Wiley, London, 1975)
16. E. Wolska, K. Stempin, O. Krasnowska-Hobbs, *Solid State Ionics* **101–103**, 527 (1997)
17. Y. Slimani, B. Unal, M.A. Almessiere, A.D. Korkmaz, S.E. Shirsath, G. Yasin, A.V. Trukhanov, A. Baykal, *Result Phys.* **17**, 103061 (2020)
18. M.A. Almessiere, Y. Slimani, H. Gungunes, S. Ali, A. Manikandan, I. Ercan, A. Baykal, A.V. Trukhanov, *Nanomaterials* **9**, 820 (2019)
19. M.A. Almessiere, Y. Slimani, M. Sertkol, M. Nawaz, A. Sad- aqat, A. Baykal, I. Ercan, B. Ozcelik, *Nanomaterials* **9**, 430 (2019)
20. A. Chauhan, R. Verma, C.G. Krishnan, R. Jayavel, K.M. Batoo, S. Hussain, R. Kumar, P. Kumar, *Appl. Phys. A* **129**(2), 117 (2023)
21. D. Parajuli, V. Raghavendra, B. Suryanarayana, P.A. Rao, N. Murali, P.V.S.K.P. Varma, R.G. Prasad, Y. Ramakrishna, K. Chandramouli, *Results Phys.* **23**, 103947 (2021)
22. D. Parajuli, N. Murali, K. Samatha, *J. Nepal Phys. Soc.* **7**, 24 (2021)
23. D. Parajuli, V.K. Vagolu, K. Chandramouli, N. Murali, K. Samatha, *J. Nepal Phys. Soc.* **7**, 14 (2021)
24. D. Parajuli, P. Taddesse, N. Murali, K. Samatha, *J. Indian Chem. Soc.* **99**, 100380 (2022)
25. S.R. Kumar, G.V. Priya, B. Aruna, M.K. Raju, D. Parajuli, N. Murali, R. Verma, K.M. Batoo, R. Kumar, P.V.L. Narayana, *Inorg. Chem. Comm.* **136**, 109132 (2022)
26. D. Parajuli, P. Taddesse, N. Murali, K. Samatha, *Appl. Phys. A Mater. Sci. Process.* **128**, 1 (2022)
27. D. Parajuli, N. Murali, A.V. Rao, A. Ramakrishna, K. Samatha, *S. Afr. J. Chem. Eng.* **42**, 106 (2022)
28. G. Aravind, M. Raghasudha, D. Ravinder, M.M. Raja, S.S. Meena, P. Bhatt, M. Hashim, *Ceram. Int.* **42**, 2941–2950 (2016)
29. R. Venkatachalapathy, C. Manoharan, M. Venkateshwarlu, G. Abd elfadeel, Y. Saddek, *Ceram. Int.* **48**, 29111–29120 (2023)
30. A.S. Chavan, B.V. Jadhav, M.R. Kadam, A.V. Mali, C.B. Mane, R.P. Patil, *Macromol. Symp.* **400**, 2100201 (2021)
31. M.P. Ghosh, S. Datta, R. Sharma, K. Tanbir, M. Kar, S. Mukhar- jee, *Mater. Sci. Eng. B* **263**, 14864 (2021)
32. M. Ramesh, G.S.N. Rao, K. Samatha, B. Parvatheeswara Rao, *Ceram. Int.* **41**, 1765 (2015)
33. B. Cullity, *Elements of X-Ray Diffraction* (Addison-Wesley Pub Co, Reading Mass, 1956)
34. R.D. Shannon, C.T. Prewitt, *Acta Crystallogr. Sect. B* **26**, 1046 (1970)
35. E.W. Gorter, J.A. Schulkes, *Phys. Rev.* **90**, 487 (1953)
36. J. Smith, H.P.J. Wijn, *Ferrites* (Philips, Eindhoven, 1959)
37. D. Ravinder, L. Balachander, Y.C. Venudhar, *Mater. Lett.* **49**, 205 (2001)
38. S.S. Bellad, R.B. Pujar, B.K. Chougule, *Mater. Chem. Phys.* **52**, 166 (1998)
39. S.A. Mazen, M.H. Abdallah, R.I. Nakhla, H.M. Zaki, F. Metawe, *Mater. Chem. Phys.* **34**, 35 (1993)
40. R.D. Waldron, *Phys. Rev.* **99**, 1727 (1955)
41. S.C. Watawe, B.D. Sutar, B.D. Sarwade, B.K. Chougule, *Int. J. Inorg. Mater.* **3**, 819 (2001)
42. S.A. Mazen, S.F. Mansour, E. Dhahri, H.M. Zaki, T.A. Elmosa- lami, *J. Alloys Compd.* **470**, 294 (2009)

43. K.B. Modi, U.N. Trivedi, M.P. Pandya, S.S. Bhatu, M.C. Chhantbar, H.H. Joshi, *Microwaves and Optoelectronics* (Anamaya Publishers, New Delhi, 2004)
44. P. Venugopal Reddy, V. Devender Reddy, J. Magn. Magn. Mater. **136**, 279 (1994)
45. R. Jasrotia, Suman, A. Verma, R. Verma, S.K. Godara, J. Ahmed, A. Mehtab, T. Ahmad, P. Puri, S. Kalia, *Ceram. Int.* **48**, 29111–29120 (2022)
46. R. Jasrotia, A. Verma, R. Verma, S. Kumar, J. Ahmad, B. Krishan, S. Kumari, A.M. Tamboli, S. Sharma, S. Kalia, J. Water Process Eng. **47**, 102785 (2022)
47. S.Y. Mulushoa, N. Murali, P. Taddesse, A. Ramkrishna, D. Parajuli, K.M. Batoo, R. Verma, R. Kumar, Y.B.S. Rao, S. Hussain, K. Samatha, *Inorg. Chem. Comm.* **138**, 109287 (2022)
48. G.V. Priya, N. Murali, M.K. Raju, B. Krishan, D. Parajuli, P. Choppera, B.C. Sekhar, R. Verma, K.M. Batoo, P.V.L. Narayana, *Appl. Phys. A* **128**, 663 (2022)
49. M. Junaid, I.A. Qazafi, M.A. Khan, S. Gulbadan, S.Z. Ilyas, H.H. Somaily, M.S. Attia, K. Ashok, H.M.N.H. Khan Asghar, *Ceram. Int.* **48**, 14307–14314 (2022)
50. B. Mali, K. Ashok, H. Sreemoolanedhan, S. Elizabeth, J. Alloy Compd. **911**, 165036 (2022)
51. M. Junaid, M.A. Khan, A. Majeed, H. Alkhalidi, M.S. Attia, M.A. Amia, M.A. Iqbal, *Ceram. Int.* **48**, 21610–21615 (2022)
52. E. De Fazio, P.G. Bercoff, S.E. Jacobo, J. Magn. Magn. Mater. **323**, 2813 (2011)
53. M. Maisnam, S. Phanjobam, H.N.K. Sarma, L. Radhapiyari Devi, O.P. Thakur, C. Prakash, *Phys. B* **352**, 86 (2004)
54. J. Cao, Y.L. Huang, Y.H. Hou, G.Q. Zhang, Z.Q. Shi, Z.C. Zhong, Z.W. Liu, *AIP Adv.* **8**, 055132 (2018)

**Publisher's Note** Springer Nature remains neutral with regard to jurisdictional claims in published maps and institutional affiliations.

Springer Nature or its licensor (e.g. a society or other partner) holds exclusive rights to this article under a publishing agreement with the author(s) or other rightsholder(s); author self-archiving of the accepted manuscript version of this article is solely governed by the terms of such publishing agreement and applicable law.